Optical Engineering

OpticalEngineering.SPIEDigitalLibrary.org

Optimization of an intrinsic coincident polarimeter and quantitative architectural comparison of different polarimeter techniques

Ruonan Yang
Pratik Sen
Brendan O'Connor
Michael Kudenov

SPIE.

Ruonan Yang, Pratik Sen, Brendan O'Connor, Michael Kudenov, "Optimization of an intrinsic coincident polarimeter and quantitative architectural comparison of different polarimeter techniques," *Opt. Eng.* **59**(2), 024111 (2020), doi: 10.1117/1.OE.59.2.024111

Optimization of an intrinsic coincident polarimeter and quantitative architectural comparison of different polarimeter techniques

Ruonan Yang,[a,*] Pratik Sen,[b] Brendan O'Connor,[b] and Michael Kudenov[a]
[a]North Carolina State University, Optical Sensing Laboratory, Department of Electrical and Computer Engineering, Raleigh, North Carolina, United States
[b]North Carolina State University, Department of Mechanical and Aerospace Engineering, Raleigh, North Carolina, United States

Abstract. Polarimeters have broad applications in remote sensing, astronomy, and biomedical imaging to measure a scene's polarization state. An intrinsic coincident (IC) full-Stokes polarimeter was previously demonstrated and optimized to achieve high temporal and spatial resolution. We optimized the IC polarimeter by introducing additional waveplates or measurement channels and compared it with existing polarimeter architectures under signal-independent Gaussian noise and signal-dependent Poisson noise. The quantitative comparison of noise variances showed that the IC and division-of-amplitude polarimeters have the lowest noise variances due to their higher signal collection ability. Both polarimeters have a factor of 2 and $\sqrt{2}$ improved signal-to-noise ratio, in the S_0 component, for Gaussian and Poisson noises, respectively, as compared to division of time, division of focal plane, and division of aperture polarimeters. While the division of amplitude and IC polarimeters outperforms other approaches, the IC polarimeter has a significantly simpler design, potentially allowing for cost-effective, high-performance polarimetric imaging.
[DOI: 10.1117/1.OE.59.2.024111]

Keywords: polarimetry; polarimetric imaging; polarization-selective devices; optimization; signal-to-noise ratio.

Paper 191427 received Oct. 15, 2019; accepted for publication Feb. 10, 2020; published online Feb. 25, 2020.

1 Introduction

Imaging polarimeters are designed to measure a scene's state of polarization and may be divided into classes based on data collection methods, including division of time (DoT),[1,2] division-of-focal-plane (DoFP),[3] division-of-aperture (DoA),[4] division-of-amplitude (DoAM),[5–7] and intrinsic coincident (IC) polarimeters.[8] A DoT polarimeter modulates a polarization element in front of a camera or detector system at least four times to obtain the full Stokes vector, resulting in a loss of temporal resolution. When used in polarization imaging, the measurement platform or targeted objects are usually in motion, so real-time detection is crucial for obtaining polarization information. DoFP, DoA, DoAM, and IC polarimeters have advantages over DoT in simultaneous measurements. DoA and DoFP polarimeters use 2×2 superpixel to obtain four measurements, yielding a loss of spatial resolution. DoAM and IC polarimeters can maintain the temporal resolution and spatial resolution simultaneously. However, DoAM polarimeters are physically larger and require multiple cameras that must be calibrated.

In our previous work,[8] we investigated the capability of organic photovoltaics (OPV) to implement a full-Stokes polarimeter. This IC polarimeter consisted of cascaded polarization-sensitive OPV and waveplates to obtain a full Stokes vector, which can maintain high temporal and potentially high spatial resolution while enabling high signal collection, if such a one-pixel IC polarimeter was miniaturized and integrated into an imaging array. This can be achieved without the use of linear polarizers, which are often employed in DoT, DoFP, and DoA

*Address all correspondence to Ruonan Yang, E-mail: ryang10@ncsu.edu

0091-3286/2020/$28.00

polarimeters. In this paper, an exhaustive optimization of a single-pixel (nonimaging) IC polarimeter design, using different configurations, was conducted and the noise performance compared to other polarimeter architectures. This analysis demonstrated that an IC polarimeter can be further improved by introducing another waveplate in front of the system or using a five-cell system. Furthermore, IC and DoAM polarimeters demonstrate a better immunity to noise than DoT, DoFP, and DoA polarimeters, due to their higher signal collection capabilities. This advantage increased signal-to-noise ratio (SNR) by a factor of 2 and $\sqrt{2}$ times in the S_0 Stokes component under Gaussian (GN) and Poisson noises (PN), respectively.

This paper is organized as follows. In Sec. 2, we introduce the design of an IC polarimeter and its Mueller matrix model. In Sec. 3, two figures of merit to evaluate a polarimeter are defined for pure GN and pure PN, under which existing polarimeter architectures DoT, DoFP, DoA, and DoAM are discussed. Different architectures for optimizing an IC polarimeter under two figures of merit are also developed in Sec. 3. In Sec. 4, we provide a quantitative comparison of existing full-Stokes polarimeter architectures. Finally, Sec. 5 concludes the paper.

2 IC Polarimeter Design

An IC polarimeter uses stacked intrinsically polarization-sensitive detectors that can be made semitransparent. One highly effective system that can achieve these device requirements is OPVs. A schematic diagram of a demonstrated polarization-sensitive semitransparent OPV cell is shown in Fig. 1(a), which has the structure of transparent substrate/transparent conduction electrodes (TCE)/charge transport layer/organic photoactive layer/charge transport layer/TCE/transparent substrate. The polarization sensitivity of an OPV detector results from applying uniaxial strain to the active layer, which aligns the polymer backbones in the direction of the strain, as depicted in Fig. 1(b). This yields a preferential absorption and subsequent photogenerated current, along the strain direction.[10] The devices can also be solutions processed onto a number of surfaces and can be effectively integrated with transparent conducting electrodes to make semitransparent detectors. Four or more such OPVs, with additional waveplates in between, form the complete IC polarimeter, enabling the measurement of full-Stokes vectors.[8] Below we discuss the IC polarimeters employing OPV cells; however, it should be noted that other detectors are possible if they can achieve the design requirements discussed herein.

To obtain the measurement matrix of an IC polarimeter, an OPV model was developed to describe its absorption and transmission behavior.[8] An OPV-based architecture is used as the basis of the model given the existing demonstrated proof of concept; however, a similar optimization of other detectors that meet the design requirements is possible. The absorption of one OPV is determined by a diattenuator to account for the different absorption between the strain direction and its orthogonal direction, which is calculated by $\mathbf{A_{OPV}} = \mathbf{M_D}\ (D_A, E_A, \theta)$ where D_A and E_A are calculated as

$$D_A = \frac{(1 - T_{\max} - \gamma) - (1 - T_{\min} - \gamma)}{(1 - T_{\max} - \gamma) + (1 - T_{\min} - \gamma)}, \tag{1}$$

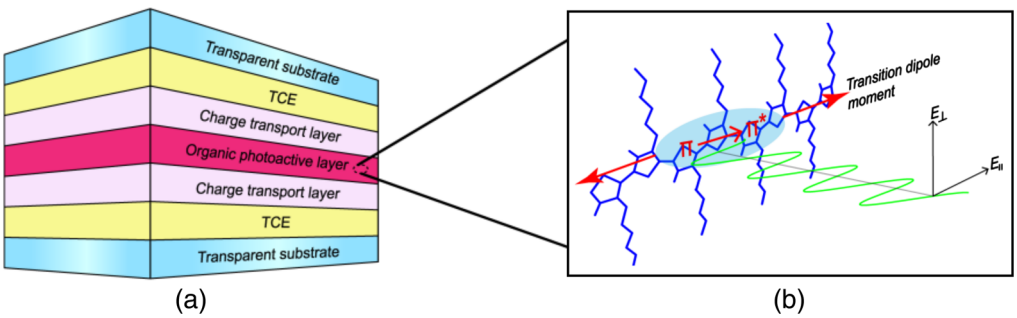

Fig. 1 (a) A schematic diagram of one OPV cell. (b) Transition dipole along the backbone of the semiconducting polymer active layer, which leads to anisotropic absorbance of polarized light.

and

$$E_A = \frac{\sqrt{(1 - T_{\max} - \gamma)(1 - T_{\min} - \gamma)}}{(1 - T_{\max} - \gamma) + (1 - T_{\min} - \gamma)}, \tag{2}$$

where $T_{\max}$, $T_{\min}$, γ, and θ are the maximum and minimum transmissions, reflectance and rotation angle of the OPV, respectively. The diattenuator matrix $\mathbf{M_D}$ (D_A, E_A, θ) can be expressed as

$$\mathbf{M_D}(D_A, E_A, \theta) = \mathbf{R}(\theta) \begin{bmatrix} 1 & D_A & 0 & 0 \\ D_A & 1 & 0 & 0 \\ 0 & 0 & 2E_A & 0 \\ 0 & 0 & 0 & 2E_A \end{bmatrix} \mathbf{R}(-\theta), \tag{3}$$

where $\mathbf{R}(\theta)$ is the rotation matrix, defined as

$$\mathbf{R}(\theta) = \begin{bmatrix} 1 & 0 & 0 & 0 \\ 0 & \cos(2\theta) & \sin(2\theta) & 0 \\ 0 & -\sin(2\theta) & \cos(2\theta) & 0 \\ 0 & 0 & 0 & 1 \end{bmatrix}. \tag{4}$$

The transmission Mueller matrix of the OPV, which describes the incident light's polarization state after transmission, is constructed using a diattenuator in series with a parallel retarder to account for the film's diattenuation and retardance, respectively, as

$$\mathbf{T_{OPV}}(D_T, E_T, \phi, \theta) = \mathbf{M_D}(D_T, E_T, \theta) \times \mathbf{M_R}(\phi, \theta), \tag{5}$$

where $\mathbf{M_D}$ (D_T, E_T, θ) and $\mathbf{M_R}$ (ϕ, θ) are Mueller matrices of diattenuator and retarder, respectively. The parameters associated with the transmission Mueller matrix are the retardance ϕ, the rotation angle θ, diattenuation D_T and E_T, which are calculated as

$$D_T = \frac{T_{\max} - T_{\min}}{T_{\max} + T_{\min}}, \tag{6}$$

and

$$E_T = \frac{\sqrt{T_{\max} T_{\min}}}{T_{\max} + T_{\min}}. \tag{7}$$

The Mueller matrix of a general retarder is defined as

$$\mathbf{M_R}(\phi, \theta) = \mathbf{R}(\theta) \begin{bmatrix} 1 & 0 & 0 & 0 \\ 0 & 1 & 0 & 0 \\ 0 & 0 & \cos(\phi) & \sin(\phi) \\ 0 & 0 & -\sin(\phi) & \cos(\phi) \end{bmatrix} \mathbf{R}(-\theta). \tag{8}$$

OPV parameters, such as $T_{\max}$, $T_{\min}$, D_T, D_A, ϕ, and γ, can be determined experimentally through characterization.

3 Optimization of the IC Polarimeter

3.1 *Figure of Merit*

Optimizing a polarimeter always seeks to structure the measurement matrix to minimize the noise variance on the Stokes vector, which is obtained from its covariance matrix $\mathbf{\Gamma^S}$ calculated from

$$\mathbf{\Gamma^S} = \mathbf{W}^{\dagger} \mathbf{\Gamma^I} [\mathbf{W}^{\dagger}]^T, \tag{9}$$

where $\mathbf{W}^{\dagger}$ is the pseudoinverse matrix of the polarimeter measurement matrix $\mathbf{W}$ and $\mathbf{\Gamma}^{\mathbf{I}}$ is the covariance matrix of the measured signal vector $\mathbf{I}$.[11] The measured signal vector $\mathbf{I} = [i_1, i_2, i_3, i_4]^T$ is the coupling between $\mathbf{W}$ and the incident Stokes vector $\mathbf{S} = [S_0, S_1, S_2, S_3]^T$, given as

$$\mathbf{I} = \mathbf{W} \cdot \mathbf{S}. \tag{10}$$

Signal-independent GN and signal-dependent PN are usually considered in evaluating a polarimeter's performance.[2,4,12–14] The measurement matrix's condition number is generally used to evaluate a polarimeter's performance under GN.[15–18] However, the condition number is only valid for evaluating performance within the same type of polarimeter and is generally insufficient to compare performance across different polarimeter architectures because it removes the system's radiometric throughput.[12] Therefore, we used the equally weighted variance (EWV)[13] as a metric to evaluate the performance of the system under GN. If GN imposed to each measurement channel is σ, the total noise variance on the Stokes vector can be calculated as

$$\text{Trace}(\mathbf{\Gamma}^{\mathbf{S}}) = \text{Trace}(\mathbf{W}^{\dagger}[\mathbf{W}^{\dagger}]^T) \cdot \sigma^2 = \text{EWV} \cdot \sigma^2. \tag{11}$$

Conversely, the noise variance of each Stokes vector, induced by signal-dependent PN, depends on the specific polarization state under test. Thus, our figure of merit under PN is the maximum variance obtained from sampled Stokes vectors. 10,000 Stokes vectors that are uniformly distributed on the Poincare sphere surface are randomly generated to evaluate noise variance under PN, as shown in Fig. 2.

For a polarimeter with N measurement channels, the maximum variance is defined as

$$\max(\sigma_{Sj}^2) = \max\left(N_{\text{ph}} \sum_{k=0}^{3} \sum_{n=1}^{N} [\mathbf{W}_{j,n}^{\dagger}]^2 \mathbf{W}_{n,k} S_k\right), \tag{12}$$

where ${\sigma_{Sj}}^2$ is the noise variance on S_j ($j = 0$, 1, 2 or 3) induced only by PN and N_{ph} is the total number of photons incident on the polarimeter.

3.2 *DoT, DoFP, DoA, DoAM, and an Ideal Polarimeter*

Before we optimize the IC polarimeter, we first investigated the noise performance of the best DoT, DoFP, DoA, and DoAM polarimeter architectures. Since DoT, DoFP, and DoA can produce a similar measurement matrix, only the DoT system was used for our comparison. Mu et al.[19] proposed three optimal configurations for a DoT variable retarder polarimeter that

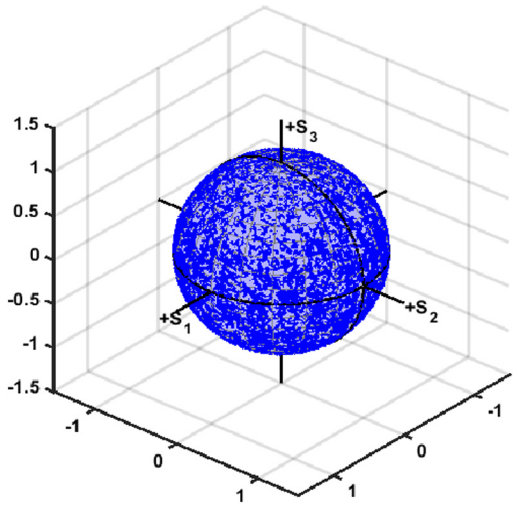

Fig. 2 10,000 Stokes vectors (blue data) are uniformly sampled across the Poincare sphere.

had maximum immunity to both PN and GN: (1) a retarder followed by a linear polarizer; (2) two retarders followed by a linear polarizer; and (3) two quarter-wave plates (QWPs) followed by a linear polarizer. Since these three configurations produced similar noise performance, only the first configuration (1) was considered in our analysis. This polarimeter had an optimal retardance of (102.2 deg and 142.1 deg) and azimuthal angles (± 71.9 deg and ± 34.95 deg). The measurement matrix produced by this set of retardance and azimuthal angles is

$$\mathbf{W}_{\mathrm{DoT}} = \begin{bmatrix} 0.1250 & 0.0722 & -0.0722 & -0.0722 \\ 0.1250 & 0.0722 & 0.0722 & 0.0722 \\ 0.1250 & -0.0722 & 0.0722 & -0.0721 \\ 0.1250 & -0.0722 & -0.0722 & 0.0721 \end{bmatrix}, \tag{13}$$

where the measurement matrix is scaled by half due to the polarizer rejecting half of light.

Meanwhile, Lara and Paterson[20] optimized Compain and Drevillon's prism-based DoAM polarimeter[5] by unconstraining the shape of the prism, thus minimizing the noise variance with the measurement matrix given as

$$\mathbf{W}_{\mathrm{DoAm}} = \begin{bmatrix} 0.2457 & -0.1324 & 0.2070 & 0 \\ 0.2457 & -0.1324 & -0.2070 & 0 \\ 0.2543 & 0.1500 & 0 & -0.2053 \\ 0.2543 & 0.1500 & 0 & 0.2053 \end{bmatrix}. \tag{14}$$

Assuming 100% light collection efficiency in the DoAM polarimeter, we normalize the matrix to make the sum of the first column equal to 1. The EWV and noise variance of the optimal DoT and prism-based DoAM under GN and PN are listed in Table 1. For PN, only the variances for the Stokes vector with the maximum noise variance are listed in the table. The noise variance is in units of σ^2 under GN and of N_{ph} under PN. DoAM has less noise variance thus higher SNR than DoT due to a higher signal collection efficiency. The sampled Stokes vectors' noise variance for DoT and DoAM under PN are plotted in Figs. 3(a) and 3(b), respectively, where only the envelope of the noise variance for S_0, S_1, S_2, and S_3 are shown for better visualization. The

Table 1 Noise variance of DoT, DoAM, and ideal polarimeter.

	GN				PN					
Conf.	Var(S_0)	Var(S_1)	Var(S_2)	Var(S_3)	Var(S_0)	Var(S_1)	Var(S_2)	Var(S_3)	EWV	Max $\sigma_{Sj}{}^2$
DoT	16.00	47.96	47.96	48.03	2.00	6.00	6.00	6.00	159.95	6.00
DoAM	4.02	12.57	11.67	11.86	1.04	3.19	4.41	4.80	40.12	4.80
Ideal	4	12	12	12	1	3	3	3	40	3

For GN, the noise variance is in the units of σ^2. For PN, the maximum noise variance of S_0, S_1, S_2, and S_3 are listed in the table, in the units of N_{ph}.

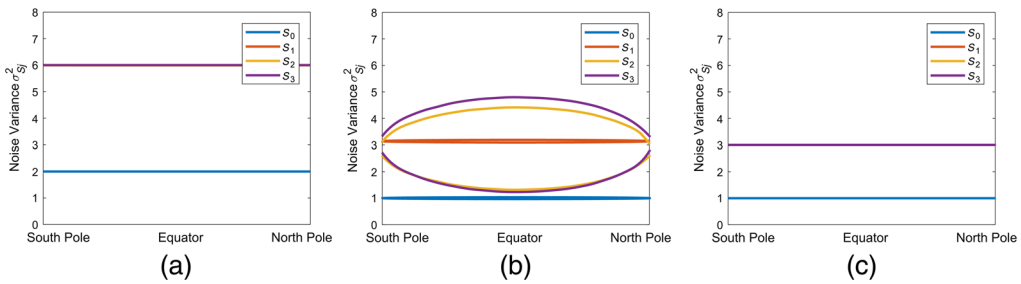

Fig. 3 Two-dimensional (2-D) envelope plot of noise variances for the sampled Stokes vector across 3-D Poincare sphere surface under PN for (a) DoT, (b) DoAM, and (c) ideal polarimeters.

horizontal axis of Figs. 3(a)–3(c) represents the location of the sampled 10,000 Stokes vectors on the Poincare sphere, as shown in Fig. 2. GN is independent of the Stokes vector; thus, only noise variance under PN is plotted. Figure 3 shows that DoT has a larger noise variance than DoAM but has a better noise equalization across all the sampled Stokes vector. For the DoAM measurement matrix per Eq. (14), the difference between the maximum and minimum noise variance is $0.07N_{\mathrm{ph}}$, $0.10N_{\mathrm{ph}}$, $3.09N_{\mathrm{ph}}$, and $3.56N_{\mathrm{ph}}$ for S_0, S_1, S_2, and S_3, respectively.

Goudail[11] proposed an ideal polarimeter that minimizes and equalizes the noise on all Stokes vectors, with the measurement matrix as

$$\mathbf{W}_{\mathrm{Ideal}} = \frac{1}{4}\begin{bmatrix} 1 & 1/\sqrt{3} & 1/\sqrt{3} & 1/\sqrt{3} \\ 1 & -1/\sqrt{3} & -1/\sqrt{3} & 1/\sqrt{3} \\ 1 & -1/\sqrt{3} & 1/\sqrt{3} & -1/\sqrt{3} \\ 1 & /\sqrt{3} & -1/\sqrt{3} & -1/\sqrt{3} \end{bmatrix}. \tag{15}$$

We listed the noise variance of this ideal polarimeter under PN and GN in Table 1 and plotted PN noise variance in Fig. 3(c). The ideal polarimeter lists the lower bound of the noise variance under GN and PN, where the minimum noise variance for S_0, S_1, S_2, and S_3 is $4\sigma^2$, $12\sigma^2$, $12\sigma^2$, and $12\sigma^2$ under GN and N_{ph}, $3N_{\mathrm{ph}}$, $3N_{\mathrm{ph}}$, and $3N_{\mathrm{ph}}$ under PN, respectively.

3.3 *Optimization of an IC Polarimeter*

In this section, different IC polarimeter structures are discussed and optimized. Optimization of an IC polarimeter using four OPV cells and two QWPs was performed under two cases in our previous discussion based on condition number metric:[8] case I: the first three OPVs are identical, and case II: the first three OPVs have different characteristics, as shown in Fig. 4(a). These two cases will be re-evaluated using the figure of merits discussed in this paper, EWV and maximum variance, in Secs. 3.3.1 and 3.3.2, respectively.

Meanwhile, in Sec. 3.3.3 and Sec. 3.3.4, we further optimize the four-cell IC polarimeter by adding an additional QWP in the front of the detectors and relaxing the waveplates' retardance by making it an additional degree of freedom for the optimization, as shown in Figs. 4(b) and 4(c), respectively. Furthermore, we also increase the number of measurement channels from 4 to 5, as shown in Fig. 4(d), which will be discussed in Sec. 3.3.5. Finally, an ideal IC polarimeter is discussed in Sec. 3.3.6.

In the following optimization, we set the same constraints that all OPVs have (a) the same responsivity R; (b) the reflectance γ of all four OPVs is zero (the reflection of OPV can be potentially reduced with highly transparent conducting electrode such as PEDOT:PSS[21]); (c) the

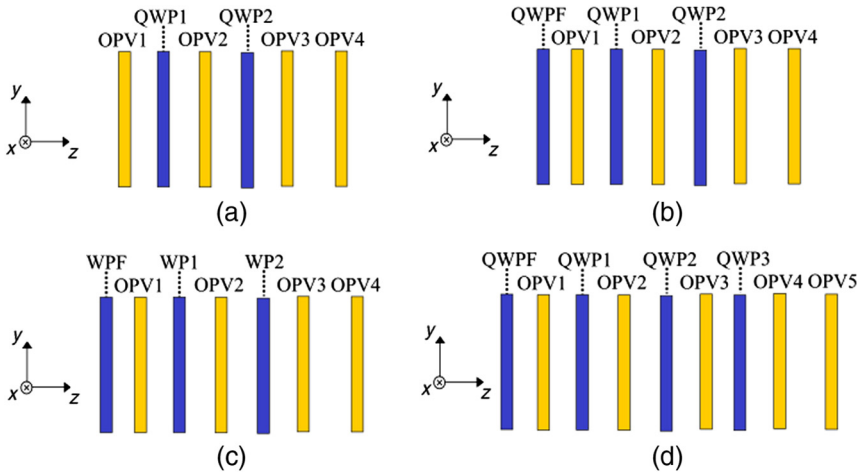

Fig. 4 IC polarimeter configurations: (a) case I and case II: four-cell (OPV) system with two QWPs. (b) Case III: four-cell system with additional QWP in front. (c) Case IV: four-cell system with retardance-relaxed waveplates. (d) Case V: five-cell ICP polarimeter.

retardance ϕ of all OPVs is zero; and (d) the last OPV absorbs all the remaining light. It should be noted that the OPV's characteristics can be modified by material selection and different process parameters typical to organic electronics fabrication.[22–24]

3.3.1 *Case I: four-cell system with identical OPVs*

As shown in Fig. 4(a), the optimization of a four-cell system, with the first three OPVs identical, is discussed in this section. The model's degrees of freedom for the optimization included the x-eigenvector's maximum transmission T_x, the diattenuation D_T of the first three OPVs, and the orientation angles of the OPVs $(\theta_1, \theta_2, \theta_3)$ and QWPs $(\theta_{R1}, \theta_{R2})$. The other parameters were either defined as constants ($\phi_1 = \phi_2 = \phi_3 = 0$ deg, $\phi_{R1} = \phi_{R2} = 90$ deg, $T_{x4} = T_{y4} = 0$, $D_{A4} = 0$, $E_{A4} = 0$, $\theta_4 = 0$ deg) or calculated via a parameter sweep (D_{A1}, D_{A2}, D_{A3}, E_{A1}, E_{A2}, E_{A3}, E_{T1}, E_{T2}, E_{T3}, T_{y1}, T_{y2}, T_{y3}) to search for regions containing minima. The optimization toolbox in MATLAB 2019a was used to minimize the objective function. The possible global minimum was found by running the optimization code with multiple starting points and choosing the output with the lowest function value. The variable model parameters are listed in vector **C**, expressed as

$$\mathbf{C} = [\theta_1, \theta_2, \theta_3, \theta_{R1}, \theta_{R2}, T_x, D_T]. \tag{16}$$

T_x and D_T are constrained from 0.1 to 0.9, and the orientation angles were restricted to span 0 deg to 360 deg.

Since GN and PM were considered separately, we created two designs that were optimized for each kind of noise. For additive GN with standard deviation σ, the EWV was minimized by the following cost function:

$$\mathbf{C} = \arg\min_{\mathbf{C}}[\mathrm{EWV}(\mathbf{W})]. \tag{17}$$

This yielded a measurement matrix as

$$\mathbf{W}_{\text{CaseI-GN}} = \begin{bmatrix} 0.3601 & -0.1950 & -0.1736 & 0 \\ 0.2295 & 0.0674 & 0.0617 & -0.1522 \\ 0.1548 & -0.0063 & 0.1117 & 0.0651 \\ 0.2547 & 0.1339 & 0.0001 & 0.0871 \end{bmatrix}. \tag{18}$$

The optimized model parameters were $\theta_1 = 20.84$ deg, $\theta_2 = 52.63$ deg, $\theta_3 = 34.03$ deg, $\theta_{R1} = 8.18$ deg, $\theta_{R2} = 0.12$ deg, $T_x = 0.90$, and $D_T = 0.41$. Optimizing under pure PN was accomplished by minimizing the maximum variance on the Stokes vector as

$$\mathbf{C} = \arg\min_{\mathbf{C}}[\max(\sigma_{Sj}^2)]. \tag{19}$$

The optimized measurement matrix was calculated as

$$\mathbf{W}_{\text{CaseI-PN}} = \begin{bmatrix} 0.3644 & -0.1729 & -0.2001 & 0 \\ 0.2480 & 0.1171 & 0.0782 & -0.1438 \\ 0.1425 & -0.0431 & 0.1022 & 0.0316 \\ 0.2450 & 0.0990 & 0.0197 & 0.1122 \end{bmatrix}. \tag{20}$$

The optimized model parameters were $\theta_1 = 24.58$ deg, $\theta_2 = 56.35$ deg, $\theta_3 = 32.62$ deg, $\theta_{R1} = 1.44$ deg, $\theta_{R2} = 10.94$ deg, $T_x = 0.90$, and $D_T = 0.42$.

The noise variances of the Stokes vectors under GN and PN are summarized in Table 2 for the two optimized matrices $\mathbf{W}_{\text{CaseI-GN}}$ and $\mathbf{W}_{\text{CaseI-PN}}$ and the noise variances under PN are shown in Figs. 5(a) and 5(b). The noise variance for S_0 follows the calculation in a conventional intensity detector: the total noise variance for S_0 under GN is the sum of the noise from all channels, which was calculated as $4\sigma^2$ and the noise variance under PN is N_{ph}, which is the number of incoming

Table 2 Noise variance under measurement matrix $\mathbf{W}_{\text{CaseI-GN}}$ and $\mathbf{W}_{\text{CaseI-PN}}$.

Measurement matrix	GN				PN				EWV	Max σ_{Sj}^2
	Var(S_0)	Var(S_1)	Var(S_2)	Var(S_3)	Var(S_0)	Var(S_1)	Var(S_2)	Var(S_3)		
$\mathbf{W}_{\text{CaseI-GN}}$	4	33.05	45.50	28.91	1	10.28	12.78	9.52	111.5	12.78
$\mathbf{W}_{\text{CaseI-PN}}$	4	40.29	41.21	30.13	1	10.66	10.66	10.66	115.6	10.66

For GN, the noise variance is in the units of σ^2. For PN, the maximum noise variance of S_0, S_1, S_2, and S_3 are listed in the table, in the units of N_{ph}.

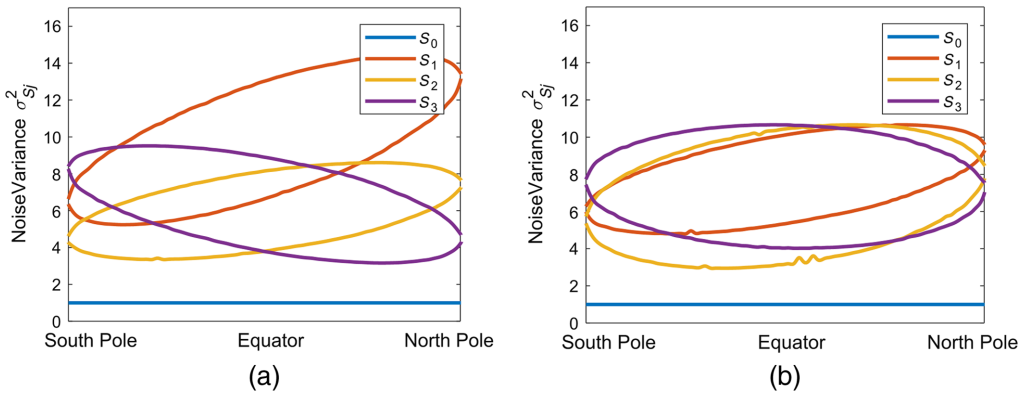

Fig. 5 2-D envelope plot of noise variances for the sampled Stokes vector across three-dimensional (3-D) Poincare sphere surface under (a) $\mathbf{W}_{\text{CaseI-GN}}$ and (b) $\mathbf{W}_{\text{CaseI-PN}}$.

photons. EWV under GN and maximum variance under PN are comparable for the two matrices in Eqs. (18) and (20). The minimum EWV under $\mathbf{W}_{\text{CaseI-GN}}$ is $111.5\sigma^2$ while $115.8\sigma^2$ under $\mathbf{W}_{\text{CaseI-PN}}$. A moderate improvement in PN performance is obtained from $\mathbf{W}_{\text{CaseI-PN}}$ with a lower maximum variance of 10.66 N_{ph}, compared with $12.78N_{\text{ph}}$ calculated from $\mathbf{W}_{\text{CaseI-GN}}$.

3.3.2 *Case II: four-cell system with different OPVs*

In this section, we optimize the previous configuration using different OPVs, which gives more freedom to improve performance. The optimization parameters are given as

$$\mathbf{C} = [\theta_1, \theta_2, \theta_3, \theta_{R1}, \theta_{R2}, T_{x1}, T_{x2}, T_{x3}, D_{T1}, D_{T2}, D_{T3}]. \tag{21}$$

Similarly, the optimized measurement matrix under GN, per Eq. (17), was calculated as

$$\mathbf{W}_{\text{CaseII-GN}} = \begin{bmatrix} 0.3061 & -0.1677 & 0.1198 & 0 \\ 0.2645 & 0.0621 & -0.0364 & -0.1882 \\ 0.2237 & 0.1431 & 0.0831 & 0.1009 \\ 0.2058 & -0.0375 & -0.1665 & 0.0873 \end{bmatrix}, \tag{22}$$

where the optimized model parameters are $\theta_1 = 162.23$ deg, $\theta_2 = 184.62$ deg, $\theta_3 = 163.96$ deg, $\theta_{R1} = 141.09$ deg, $\theta_{R2} = 140.47$ deg, $T_{x1} = T_{x2} = T_{x3} = 0.90$, $D_{T1} = 0.30$, $D_{T2} = 0.46$, and $D_{T3} = 0.9$. Meanwhile, the optimized measurement matrix under PN, per Eq. (19), was calculated as

$$\mathbf{W}_{\text{CaseII-PN}} = \begin{bmatrix} 0.3059 & -0.1757 & 0.1045 & 0 \\ 0.2671 & 0.0047 & -0.1133 & -0.1665 \\ 0.2258 & 0.1683 & 0.1011 & 0.0032 \\ 0.2012 & 0.0027 & -0.0923 & 0.1633 \end{bmatrix}, \tag{23}$$

Table 3 Noise variance under measurement matrix $\mathbf{W}_{\text{CaseII-GN}}$ and $\mathbf{W}_{\text{CaseII-PN}}$.

Measurement matrix	GN				PN				EWV	Max $\sigma_{Sj}{}^2$
	Var(S_0)	Var(S_1)	Var(S_2)	Var(S_3)	Var(S_0)	Var(S_1)	Var(S_2)	Var(S_3)		
$\mathbf{W}_{\text{CaseII-GN}}$	4	18.82	20.19	18.96	1	6.55	6.74	6.53	61.94	6.74
$\mathbf{W}_{\text{CaseII-PN}}$	4	17.21	23.97	18.70	1	6.23	6.21	6.23	63.89	6.23

For GN, the noise variance is in the units of σ^2. For PN, the maximum noise variance of S_0, S_1, S_2, and S_3 are listed in the table, in the units of N_{ph}.

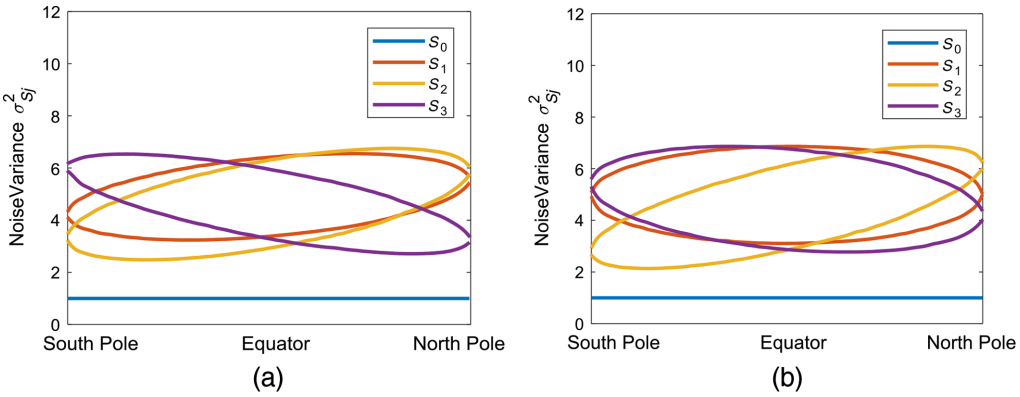

Fig. 6 2-D envelope plot of noise variances for the sampled Stokes vector across 3-D Poincare sphere surface under (a) $\mathbf{W}_{\text{CaseII-GN}}$ and (b) $\mathbf{W}_{\text{CaseII-PN}}$.

where the optimized model parameters are $\theta_1 = 164.63$ deg, $\theta_2 = 174.45$ deg, $\theta_3 = 130.51$ deg, $\theta_{R1} = 114.39$ deg, $\theta_{R2} = 131.31$ deg, $T_{x1} = T_{x2} = T_{x3} = 0.90$, $D_{T1} = 0.29$, $D_{T2} = 0.48$, and $D_{T3} = 0.9$.

Using different OPVs to construct the polarimeter results in a reduction of 44% in total noise variance under GN and 41% for the maximum variance under PN, compared with case I. These results are summarized in Table 3 and shown in Figs. 6(a) and 6(b).

3.3.3 *Case III: four-cell system with an additional QWP*

Optimization in this section focuses on adding a QWP in front of the IC polarimeter, enabling OPV1 to gain sensitivity in measuring the S_3 Stokes parameter. Additional model parameters for this configuration are the first QWP's orientation angle θ_{RF}. The optimization parameters are given as

$$\mathbf{C} = [\theta_1, \theta_2, \theta_3, \theta_{RF}, \theta_{R1}, \theta_{R2}, T_{x1}, T_{x2}, T_{x3}, D_{T1}, D_{T2}, D_{T3}]. \tag{24}$$

The optimized measurement matrix under GN was calculated as

$$\mathbf{W}_{\text{CaseIII-GN}} = \begin{bmatrix} 0.3061 & -0.1207 & -0.1151 & 0.1210 \\ 0.2645 & -0.1102 & 0.1261 & -0.1121 \\ 0.2237 & 0.1265 & 0.1011 & 0.1065 \\ 0.2058 & 0.1044 & -0.1121 & -0.1153 \end{bmatrix}. \tag{25}$$

The optimized model parameters were calculated to be $\theta_1 = 183.85$ deg, $\theta_2 = 195.19$ deg, $\theta_3 = 148.32$ deg, $\theta_{RF} = 21.82$ deg, $\theta_{R1} = 136.48$ deg, $\theta_{R2} = 150.78$ deg, $T_{x1} = T_{x2} = T_{x3} = 0.90$, $D_{T1} = 0.30$, $D_{T2} = 0.46$, and $D_{T3} = 0.9$. Optimization under PN produced the measurement matrix

Table 4 Noise variance under measurement matrix $\mathbf{W}_{\text{CaseIII-GN}}$ and $\mathbf{W}_{\text{CaseIII-PN}}$.

Measurement matrix	GN				PN				EWV	Max $\sigma_{Sj}{}^2$
	Var(S_0)	Var(S_1)	Var(S_2)	Var(S_3)	Var(S_0)	Var(S_1)	Var(S_2)	Var(S_3)		
$\mathbf{W}_{\text{CaseIII-GN}}$	4	19.03	19.40	19.51	1	5.27	5.11	5.18	61.94	5.27
$\mathbf{W}_{\text{CaseIII-PN}}$	4	18.71	20.07	19.56	1	5.08	5.08	5.08	62.34	5.08

For GN, the noise variance is in the units of σ^2. For PN, the maximum noise variance of S_0, S_1, S_2, and S_3 are listed in the table, in the units of N_{ph}.

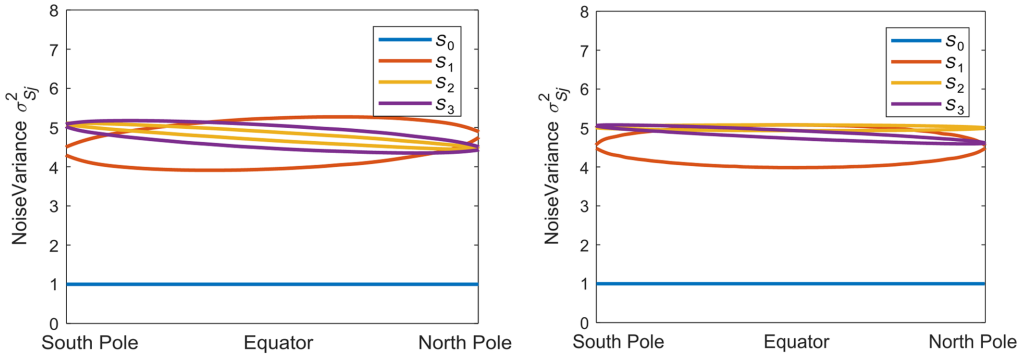

Fig. 7 2-D envelope plot of noise variances for the sampled Stokes vector across 3-D Poincare sphere surface under (a) $\mathbf{W}_{\text{CaseIII-GN}}$ and (b) $\mathbf{W}_{\text{CaseIII-PN}}$.

$$\mathbf{W}_{\text{CaseIII-PN}} = \begin{bmatrix} 0.2980 & -0.1144 & -0.1144 & 0.1119 \\ 0.2648 & -0.1164 & 0.1139 & -0.1160 \\ 0.2274 & 0.1167 & 0.1094 & 0.1146 \\ 0.2098 & 0.1163 & -0.1089 & -0.1105 \end{bmatrix}, \tag{26}$$

with optimized model parameters of $\theta_1 = 185.02$ deg, $\theta_2 = 196.97$ deg, $\theta_3 = 148.50$ deg, $\theta_{RF} = 22.22$ deg, $\theta_{R1} = 136.39$ deg, $\theta_{R2} = 152.21$ deg, $T_{x1} = T_{x2} = T_{x3} = 0.90$, $D_{T1} = 0.28$, $D_{T2} = 0.46$, and $D_{T3} = 0.89$. These results are summarized in Table 4, and noise variances under PN are plotted in Figs. 7(a) and 7(b) for $\mathbf{W}_{\text{CaseIII-GN}}$ and $\mathbf{W}_{\text{CaseIII-PN}}$, respectively. Comparing with case II, the total noise variance shows no improvement under GN, which is $61.94\sigma^2$ under both cases. However, the maximum noise variance under PN was reduced from $6.23N_{\text{ph}}$ to $5.08N_{\text{ph}}$.

3.3.4 *Case IV: four-cell system with retardance-relaxed waveplates*

In order to use commercially available off-the-shelf components, the retarders used in the previous optimization were configured as standard QWPs. Consequently, we optimized the IC polarimeter by including the waveplates' retardance as a degree of freedom, as illustrated previously in Fig. 4(c). The optimization parameters are given as

$$\mathbf{C} = [\theta_1, \theta_2, \theta_3, \theta_{RF}, \theta_{R1}, \theta_{R2}, T_{x1}, T_{x2}, T_{x3}, D_{T1}, D_{T2}, D_{T3}, \phi_{RF}, \phi_{R1}, \phi_{R2}], \tag{27}$$

where ϕ_{RF}, ϕ_{R1}, and ϕ_{R2} are the retardances for WPF, WP1, and WP2, respectively. Minimizing the EWV, under GN, yielded the optimized measurement matrix

$$\mathbf{W}_{\text{CaseIV-GN}} = \begin{bmatrix} 0.3061 & -0.1215 & -0.1168 & 0.1186 \\ 0.2645 & -0.1098 & 0.1222 & -0.1167 \\ 0.2237 & 0.1208 & 0.1053 & 0.1090 \\ 0.2058 & 0.1104 & -0.1107 & -0.1110 \end{bmatrix}, \tag{28}$$

with optimized model parameters of $\theta_1 = 184.24$ deg, $\theta_2 = 195.71$ deg, $\theta_3 = 147.59$ deg, $\theta_{RF} = 21.82$ deg, $\theta_{R1} = 135.82$ deg, $\theta_{R2} = 151.25$ deg, $T_{x1} = T_{x2} = T_{x3} = 0.90$, $D_{T1} = 0.30$, $D_{T2} = 0.46$, $D_{T3} = 0.9$, $\phi_{RF} = 90.33$ deg, $\phi_{R1} = 91.39$ deg, and $\phi_{R2} = 90.86$ deg. Optimization under PN produced the measurement matrix

$$\mathbf{W}_{\text{CaseIV-PN}} = \begin{bmatrix} 0.2966 & -0.1167 & -0.1122 & 0.1115 \\ 0.2650 & -0.1163 & 0.1137 & -0.1161 \\ 0.2279 & -0.1172 & 0.1094 & 0.1148 \\ 0.2105 & 0.1158 & -0.1109 & -0.1101 \end{bmatrix}, \tag{29}$$

with optimized model parameters of $\theta_1 = 184.54$ deg, $\theta_2 = 196.23$ deg, $\theta_3 = 147.08$ deg, $\theta_{RF} = 21.82$ deg, $\theta_{R1} = 135.31$ deg, $\theta_{R2} = 151.44$ deg, $T_{x1} = T_{x2} = T_{x3} = 0.90$, $D_{T1} = 0.28$, $D_{T2} = 0.46$, $D_{T3} = 0.89$, $\phi_{RF} = 90.32$ deg, $\phi_{R1} = 90.67$ deg, and $\phi_{R2} = 90.84$ deg. The noise performance, calculated by the optimized two matrices per Eqs. (28) and (29), is listed in Table 5, and the PN variances of the estimated Stokes vectors are shown in Figs. 8(a) and 8(b), respectively. This shows that there is no significant improvement by relaxing the waveplates' retardances compared with case III with the minimum total noise variance of $61.94\sigma^2$ under GN and the optimized maximum variance under PN of $5.08N_{\text{ph}}$ for case III and case IV.

3.3.5 *Case V: five-cell system*

The final optimization case was selected by adding an OPV cell and QWP, as depicted previously in Fig. 4(d). Minimizing the EWV, under GN, produced an optimized measurement matrix

Table 5 Noise variance under measurement matrix $\mathbf{W}_{\text{CaseIV-GN}}$ and $\mathbf{W}_{\text{CaseIV-PN}}$.

Measurement matrix	GN				PN				EWV	Max $\sigma_{Sj}{}^2$
	Var(S_0)	Var(S_1)	Var(S_2)	Var(S_3)	Var(S_0)	Var(S_1)	Var(S_2)	Var(S_3)		
$\mathbf{W}_{\text{CaseIV-GN}}$	4	19.04	19.42	19.48	1	5.21	5.05	5.11	61.94	5.21
$\mathbf{W}_{\text{CaseIV-PN}}$	4	18.71	20.10	19.59	1	5.08	5.08	5.08	62.40	5.08

For GN, the noise variance is in the units of σ^2. For PN, the maximum noise variance of S_0, S_1, S_2, and S_3 are listed in the table, in the units of N_{ph}.

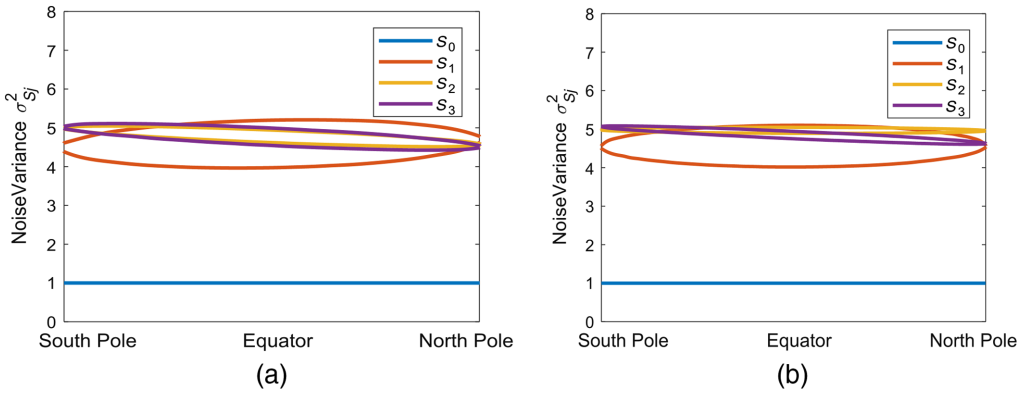

Fig. 8 2-D envelope plot of noise variances for the sampled Stokes vector across 3-D Poincare sphere surface under (a) $\mathbf{W}_{\text{CaseIV-GN}}$ and (b) $\mathbf{W}_{\text{CaseIV-PN}}$.

$$\mathbf{W}_{\text{CaseV-GN}} = \begin{bmatrix} 0.3060 & 0.1187 & 0.1158 & 0.1221 \\ 0.2644 & -0.1859 & -0.0164 & 0.0756 \\ 0.2238 & -0.0086 & 0.0757 & -0.1783 \\ 0.2041 & 0.0756 & -0.1748 & -0.0193 \\ 0.0017 & 0.0001 & -0.0003 & -0.0001 \end{bmatrix}, \tag{30}$$

with the optimized parameters $\theta_1 = 93.97$ deg, $\theta_2 = 30.95$ deg, $\theta_3 = 167.76$ deg, $\theta_4 = 75.26$ deg, $\theta_{RF} = 112.14$ deg, $\theta_{R1} = 50.37$ deg, $\theta_{R2} = 76.53$ deg, $\theta_{R3} = 53.98$ deg, $T_{x1} = T_{x2} = T_{x3} = 0.90$, $T_{x4} = 0.1$, $D_{T1} = 0.30$, $D_{T2} = 0.46$, $D_{T3} = 0.90$, and $D_{T4} = 0.90$. Meanwhile, the maximum variance under PN demonstrated a small improvement, where the optimized measurement matrix

$$\mathbf{W}_{\text{CaseV-PP}} = \begin{bmatrix} 0.3013 & 0.1134 & 0.1140 & 0.1211 \\ 0.2566 & -0.1102 & -0.1084 & 0.1131 \\ 0.2283 & -0.1096 & 0.1147 & -0.1164 \\ 0.1096 & 0.0774 & -0.0410 & -0.0608 \\ 0.1041 & 0.0290 & -0.0793 & -0.0569 \end{bmatrix}, \tag{31}$$

with the optimized model parameters $\theta_1 = 94.09$ deg, $\theta_2 = 51.83$ deg, $\theta_3 = 188.99$ deg, $\theta_4 = 40.13$ deg, $\theta_{RF} = 112.58$ deg, $\theta_{R1} = 52.09$ deg, $\theta_{R2} = 97.39$ deg, $\theta_{R3} = 53.99$ deg, $T_{x1} = T_{x2} = T_{x3} = T_{x4} = 0.90$, $D_{T1} = 0.29$, $D_{T2} = 0.44$, $D_{T3} = 0.9$, and $D_{T4} = 0.82$. A summary of these results is presented in Table 6. While this solution minimizes the maximum variance, it introduces more noise into the system by increasing the measurement channels, yielding an increased EWV. The PN variances of the estimated Stokes vectors based on two matrices per Eqs. (30) and (31), are plotted in Figs. 9(a) and 9(b), respectively.

Table 6 Noise variance under measurement matrix $\mathbf{W}_{\text{CaseV-GN}}$ and $\mathbf{W}_{\text{CaseV-PN}}$.

Measurement matrix	GN				PN				EWV	Max σ_{Sj}^2
	Var(S_0)	Var(S_1)	Var(S_2)	Var(S_3)	Var(S_0)	Var(S_1)	Var(S_2)	Var(S_3)		
$\mathbf{W}_{\text{CaseV-GN}}$	4.01	18.42	20.35	19.24	1	6.89	7.03	7.03	62.03	7.03
$\mathbf{W}_{\text{CaseV-PN}}$	5.00	24.90	24.28	24.06	1	5.00	5.00	5.00	78.25	5.00

For GN, the noise variance is in the units of σ^2. For PN, the maximum noise variance of S_0, S_1, S_2, and S_3 are listed in the table, in the units of N_{ph}.

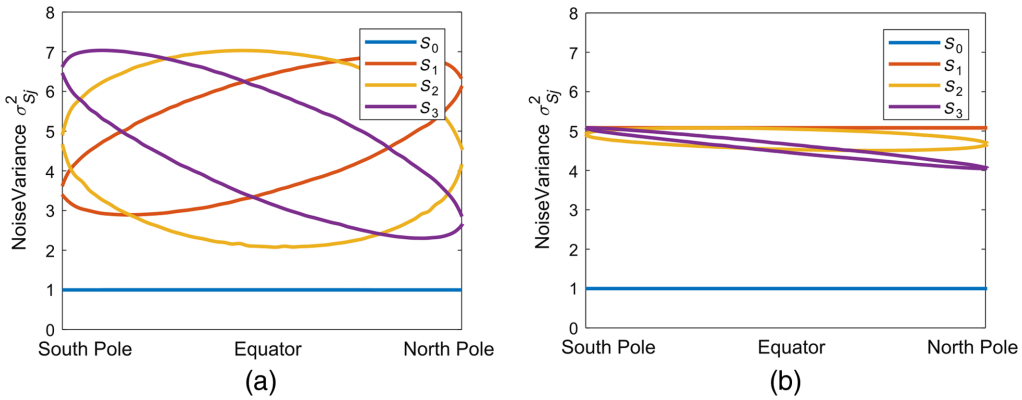

Fig. 9 2-D envelope plot of noise variances for the sampled Stokes vector across 3-D Poincare sphere surface under (a) $\mathbf{W}_{\text{CaseV-GN}}$ and (b) $\mathbf{W}_{\text{CaseV-PN}}$.

Table 7 Noise variance under measurement matrix $\mathbf{W}_{\text{Ideal}}$ and $\mathbf{W}_{\text{Ideal-IC}}$.

Measurement matrix	GN				PN				EWV	Max $\sigma_{Sj}{}^2$
	Var(S_0)	Var(S_1)	Var(S_2)	Var(S_3)	Var(S_0)	Var(S_1)	Var(S_2)	Var(S_3)		
$\mathbf{W}_{\text{Ideal}}$	4	12	12	12	1	3	3	3	40	3
$\mathbf{W}_{\text{Ideal-IC}}$	4	12.03	12.03	12.03	1	3.01	3.01	3.01	40.09	3.01

For GN, the noise variance is in the units of σ^2. For PN, the maximum noise variance of S_0, S_1, S_2, and S_3 are listed in the table, in the units of N_{ph}.

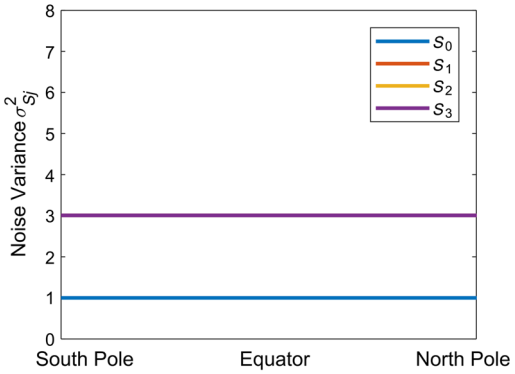

Fig. 10 Noise variances of the sampled Stokes vector under PN for ideal IC polarimeter.

3.3.6 *Case VI: ideal IC polarimeter*

In our previous optimization, we constrain both T_x and D_T from 0.1 to 0.9 for optimization and achieve a minimum EWV 61.94 in cases II, III, and IV and a minimum–maximum variance under PN of $5N_{\text{ph}}$ in case V. In this section, we relaxed T_x and D_T to allow for the ideal situation, where these values can span 0 to 1 and perform the optimization using the case IV architecture. The model parameters were $\theta_1 = 164.55$ deg, $\theta_2 = 162.82$ deg, $\theta_3 = 126.05$ deg, $\theta_{RF} = 46.27$ deg, $\theta_{R1} = 105.62$ deg, $\theta_{R2} = 198.04$ deg, $T_{x1} = T_{x2} = T_{x3} = 1$, $D_{T1} = 0.33$, $D_{T2} = 0.50$, $D_{T3} = 1$, $\phi_{RF} = 136.22$ deg, $\phi_{R1} = 103.86$ deg, and $\phi_{R2} = 60.75$ deg resulted in an ideal IC polarimeter with a measurement matrix

$$\mathbf{W}_{\text{Ideal-IC}} = \begin{bmatrix} 0.25 & 0.1441 & 0.1441 & 0.1441 \\ 0.25 & -0.1441 & -0.1441 & 0.1441 \\ 0.25 & -0.1441 & 0.1441 & -0.1441 \\ 0.25 & 0.1441 & -0.1441 & -0.1441 \end{bmatrix}, \tag{32}$$

which has a similar noise performance as an ideal polarimeter per Eq. (15), as listed in Table 7 and shown in Fig. 10.

4 Comparison of Different Polarimeter Architectures

Figure 11 summarizes the ideal, DoT, DoAM, and best IC polarimeters under PN spanning all cases, which are denoted as ICP-I to ICP-VI, respectively. These data demonstrate that the DoAM and IC polarimeters had a smaller EWV than DoT since the signal collection ability in DoAM and IC polarimeters is nearly 100%, while the polarizer annihilated half of the light in DoT. Considering GN only, the noise variance of S_0, when using a four-channel IC polarimeter, is four times smaller than DoT, which yields a factor of 2 improvements in the SNR. Under PN, the noise variance in S_0 is two times smaller in the DoAM and IC polarimeters, indicating a $\sqrt{2}$ improvement in SNR in S_0. The ideal polarimeter gives the minimum total noise

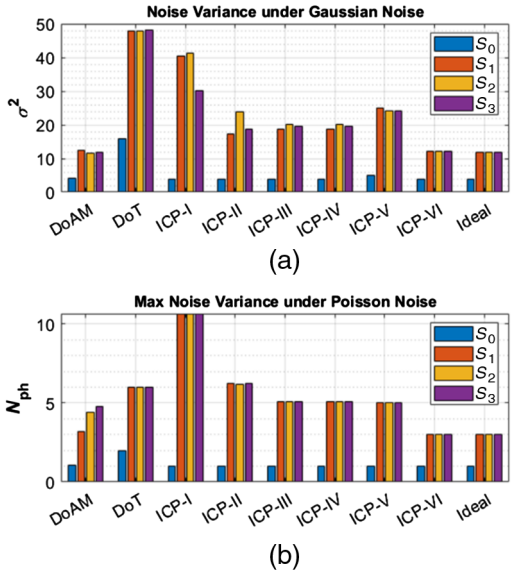

Fig. 11 Noise variance comparison of ideal, DoT, DoAM, and ICP polarimeters. (a) Noise variance of S_0, S_1, S_2, and S_3 under GN. (b) Maximum noise variance of S_0, S_1, S_2, and S_3 under PN.

variance under GN of $40\sigma^2$ and a minimum max noise variance under PN of $3N_{\text{ph}}$. The ideal IC polarimeter in case-VI has the potential to achieve similar noise variance compared to the ideal polarimeter. However, the optimized parameters of an ideal IC polarimeter with maximum transmission and diattenuation of 100% are not practical using existing material systems.

These results assist in providing guidelines for future polarization-sensitive detectors to maximize the performance of IC imaging polarimetry. Most clearly, there is a need to maximize the transmittance of the detectors in the electric field direction of low absorption by the active layers (T_x in our reference frame). For instance, the optimization consistently set the transmittance in the T_x direction to hit the maximum bound of 0.9. This suggested that the conducting electrodes must have maximal optical transmission. Alternatively, the electrodes can be moved out of the optical path by introducing other detection elements, such as phototransistors.[25] An additional design requirement that becomes evident is the need to have each OPVs' diattenuation separately optimized. This requires the optical anisotropy of the active layer to be tunable; a feature that is possible with strain aligning polymer-based detectors.[10,23] In this situation (studied in case II), the diattenuation of cells 1, 2, and 3 gradually increased, spanning values of 0.3, 0.46, and 0.9, respectively. The strain alignment approach can meet the diattenuation demand of 0.45; however, achieving a diattenuation of 0.9 requires a very high degree of orientational order of the polymers. Thus, alternative alignment methods to achieve this level of order may be necessary. While achieving an ideal IC polarimeter is not possible, given a transmittance of 1 if not possible with any refractive index change of the detector element, we believe that OPV cells are well-equipped to approach this limit.

5 Conclusion

IC polarimeters were optimized for different configurations in this paper. This included (1) case I: a four-cell system with the first three OPVs identical; (2) case II: a four-cell system with different OPVs; (3) case III: a four-cell system with an additional QWP in front; (4) case IV: a four-cell system containing waveplates with arbitrary retardance values; (5) case V: a five-cell system; and (6) case VI: ideal IC polarimeter. It was demonstrated that cases III and IV had the best structure under GN with a total noise variance $61.94\sigma^2$ while case V had the best structure under PN with a maximum noise variance of $5N_{\text{ph}}$; however, this was only marginally better than the $5.08N_{\text{ph}}$ obtained by the four-cell systems in cases III and IV. However, introducing the additional measurement channel in case V yields a larger variance under GN. Therefore, there is a tradeoff to designing an IC polarimeter when considering GN and PN

limited regimes. Furthermore, we demonstrated a quantitative comparison among the existing optimal polarimeters, which indicated that the IC and DoAM polarimeters have better noise immunity than DoT, DoFP, and DoA due to their higher signal collection ability. This yielded a twofold improved SNR in S_0 under GN and a $\sqrt{2}$-factor improvement under PN. An ideal IC polarimeter can achieve small noise variance as an ideal polarimeter but it depends on future technology development and is not practical from existing material systems. The optimization analysis in this paper shows that IC polarimeters could represent high-performance imaging polarimeters and provides design guidelines to maximize performance within these new detector systems.

Acknowledgments

This material was based on work supported by the National Science Foundation under Grant Nos. ECCS-1407885 and ECCS-1809753.

References

1. A. Ambirajan and D. C. Look Jr., "Optimum angles for a polarimeter: part I," *Opt. Eng.* **34**(6), 1651 (1995).
2. J. S. Tyo, "Noise equalization in Stokes parameter images obtained by use of variable-retardance polarimeters," *Opt. Lett.* **25**(16), 1198 (2000).
3. R. Perkins and V. Gruev, "Signal-to-noise analysis of Stokes parameters in division of focal plane polarimeters," *Opt. Express* **18**(25), 25815 (2010).
4. T. Mu et al., "Error analysis of single-snapshot full-Stokes division-of-aperture imaging polarimeters," *Opt. Express* **23**(8), 10822 (2015).
5. E. Compain and B. Drevillon, "Broadband division-of-amplitude polarimeter based on uncoated prisms," *Appl. Opt.* **37**(25), 5938 (1998).
6. R. M. A. Azzam, "Beam-splitters for the division-of-amplitude photopolarimeter," *Opt. Acta: Int. J. Opt.* **32**(11), 1407–1412 (1985).
7. S. Krishnan, "Calibration, properties, and applications of the division-of-amplitude photopolarimeter at 6328 and 1523 nm," *J. Opt. Soc. Am. A* **9**(9), 1615 (1992).
8. R. Yang et al., "Intrinsic coincident full-Stokes polarimeter using stacked organic photovoltaics," *Appl. Opt.* **56**(6), 1768 (2017).
9. S. G. Roy et al., "Intrinsic coincident linear polarimetry using stacked organic photovoltaics," *Opt. Express* **24**(13), 14737 (2016).
10. O. Awartani, M. W. Kudenov, and B. T. O'Connor, "Organic photovoltaic cells with controlled polarization sensitivity," *Appl. Phys. Lett.* **104**(9), 093306 (2014).
11. F. Goudail, "Noise minimization and equalization for Stokes polarimeters in the presence of signal-dependent Poisson shot noise," *Opt. Lett.* **34**(5), 647 (2009).
12. N. Hagen and Y. Otani, "Stokes polarimeter performance: general noise model and analysis," *Appl. Opt.* **57**(15), 4283 (2018).
13. F. Goudail, "Equalized estimation of Stokes parameters in the presence of Poisson noise for any number of polarization analysis states," *Opt. Lett.* **41**(24), 5772 (2016).
14. M. R. Foreman and F. Goudail, "On the equivalence of optimization metrics in Stokes polarimetry," *Opt. Eng.* **58**(8), 082410 (2019).
15. P. Lemaillet, S. Rivet, and B. Le Jeune, "Optimization of a snapshot Mueller matrix polarimeter," *Opt. Lett.* **33**(2), 144 (2008).
16. R. M. A. Azzam, I. M. Elminyawi, and A. M. El-Saba, "General analysis and optimization of the four-detector photopolarimeter," *J. Opt. Soc. Am. A* **5**(5), 681 (1988).
17. S. N. Savenkov, "Optimization and structuring of the instrument matrix for polarimetric measurements," *Opt. Eng.* **41**(5) (2002).
18. K. M. Twietmeyer and R. A. Chipman, "Optimization of Mueller matrix polarimeters in the presence of error sources," *Opt. Express* **16**(15), 11589 (2008).
19. T. Mu et al., "Optimal configurations of full-Stokes polarimeter with immunity to both Poisson and Gaussian noise," *J. Opt.* **18**(5), 055702 (2016).

20. D. Lara and C. Paterson, "Stokes polarimeter optimization in the presence of shot and Gaussian noise," *Opt. Express* **17**(23), 21240 (2009).
21. K. Ellmer, "Past achievements and future challenges in the development of optically transparent electrodes," *Nat. Photonics* **6**(12), 809–817 (2012).
22. B. O'Connor et al., "Anisotropic structure and charge transport in highly strain-aligned regioregular poly(3-hexylthiophene)," *Adv. Funct. Mater.* **21**(19), 3697–3705 (2011).
23. B. T. O'Connor, O. M. Awartani, and N. Balar, "Morphological considerations of organic electronic films for flexible and stretchable devices," *MRS Bull.* **42**(02), 108–114 (2017).
24. P. Sen et al., "Panchromatic all-polymer photodetector with tunable polarization sensitivity," *Adv. Opt. Mater.* **7**, 1801346 (2018).
25. K.-J. Baeg et al., "Organic light detectors: photodiodes and phototransistors," *Adv. Mater.* **25**(31), 4267–4295 (2013).

Ruonan Yang received her BS degree in optical engineering from Zhejiang University, Hangzhou, China, in 2014, and is currently a PhD student in electrical and computer engineering at North Carolina State University. Her research at the Optical Sensing Laboratory is focused on imaging and polarimetry.

Pratik Sen received his BS degree in mechanical engineering at North Carolina State University in 2014 and continued his PhD at North Carolina State University. His research is focused on fabrication and characterization techniques associated with organic photovoltaics and photodetectors.

Brendan O'Connor is an associate professor in mechanical and aerospace engineering at North Carolina State University. His research focuses on fabrication, characterization, and modeling of organic electronic devices. His current research interests in Dr. O'Connor's group include the development of robust flexible and stretchable devices, producing devices with unique capabilities, and establishing scalable processing methods. His devices of interest include solar cells, photodetectors, transistors, and thermoelectronics.

Michael Kudenov received his BS degree in electrical engineering from the University of Alaska in 2005 and his PhD in optical sciences from University of Arizona in 2009. He is currently an associate professor in the Electrical and Computer Engineering Department at North Carolina State University. His research focuses on visible-light and thermal-infrared spectrometer, interferometer, and polarimeter systems development and calibration. Applications span chemical identification, remote sensing, fluorescence imaging, polarimetry, spectroscopy, ultraspectral imaging, and optical testing.